PAPER Nr.: 69

TIME-DOMAIN AEROELASTIC SIMULATIONS WITH A FLAPPING-TORSION BLADE MODEL INCLUDING DYNAMIC STALL EFFECTS

BY

F. NITZSCHE

DLR - INSTITUTE OF STRUCTURAL MECHANICS
BRAUNSCHWEIG, GERMANY

TWENTIETH EUROPEAN ROTORCRAFT FORUM
OCTOBER 4 - 7, 1994 AMSTERDAM

Printed by the Technical Highschool Haarlem

Time-Domain Aeroelastic Simulations with a Flapping-Torsion Blade Model Including Dynamic Stall Effects

Fred Nitzsche
DLR - Institute of Structural Mechanics
Lilienthalplatz 7, D-38108 Braunschweig, FRG

Abstract

A basic study on the forced aeroelastic response characteristics of a bearingless rotor blade in forward flight is performed. An aeroelastic time-domain model which incorporates the blade elastic flapping and torsion degrees of freedom, and a more complete aerodynamic formulation including dynamic stall, compressibility and free wake effects is developed using the integrating-matrix method. The interaction between dynamic and aerodynamic modes is investigated in detail, leading to the conclusion that a substantial reduction in the vibration levels at the critical rotor frequencies multiple of the number of blades may be achieved if the dynamic and aerodynamic characteristic frequencies are well separated in the spectrum. The study also suggests that the active control techniques based on tailoring the relative position of the complex poles (damping and/or frequency) associated with the aeroelastic modes of a single blade can provide a basic and efficient solution for the helicopter's airframe/rotor vibration problem.

1. Introduction

The objective of this study is to investigate some basic aspects of the open-loop aeroelastic response characteristics of bearingless rotors in forward flight. A simplified dynamic model of a single blade with a more complete aerodynamic formulation including dynamic stall, compressibility and free wake effects is developed. As a first approach to the problem, the aerodynamic damping due to the out-of-phase unsteady loads is not included, but it can be easily introduced in a more sophisticated analysis. Moreover, the present model can be extended to perform time-domain aeroelastic response simulations of the complete, multi-blade rotor. Closed-loop analyses of individual-blade-control systems can also be performed with minimal additional computation effort. As a case study, the aeroelastic response of a single blade of the two-meter diameter, four-blade rotor model which was extensively tested for its aerodynamic characteristics in the German-Dutch Wind Tunnel (DNW) in December 1992 is simulated.

In the previous investigations an aeroelastic model of a bearingless rotary wing including both the elastic flatwise bending and the torsion degrees of freedom was described [1], [2]. This model was developed using the integrating matrix method where the blade local properties (i.e. mass, stiffness and aerodynamics) are defined at n discrete points along the structure. The integrating matrix is a co-located semi-analytical method to solve *linear* differential equations with generic boundary conditions [3]. It uses high-order polynomial interpolations to approximate the required variation in the blade local

properties. Integrating and differentiating matrix operators of size *nxn* are constructed to handle the mathematical modelling situations usually found in an aeroelastic formulation. The method can be extended to deal with differential equations with periodic coefficients and control variables as well [1], [2], [4]. The most interesting feature of the method is its ability to solve a complex problem such as the elastic rotary wing using a semi-analytical approach. Simple algebraic manipulations eliminate the spatial independent variable and reduce the blade governing differential equations to a standard time-domain form. The equations may be then either directly integrated in time or decomposed in a modal subspace as an intermediate step. Using the latter approach, the order of the problem is further decreased and very efficient computational results are obtained.

2. Aeroelastic Model

The single blade governing differential equations (in non-dimensional form, [1]) are cast in a state vector form where the dependent variables are the cross-section flatwise bending M, shear resultant H, bending slope φ, bending displacement w, torque τ and torsion deformation θ. The independent variables are the normalized (with respect to the rotor radius R) spanwise coordinate r and time, or more precisely the azimuth angle $\psi=\Omega t$. Dots denote the time differentiation and primes the spatial differentiation:

$$
\begin{aligned}
M' &= H + \nu T \varphi \\
H' &= \nu m \ddot{w} - F_w \\
\varphi' &= D^*_{11} M + D^*_{13} \tau \\
w' &= -\varphi \\
\tau' &= \nu m k_\theta^2 \left(\theta + \ddot{\theta}\right) - M_\theta \\
\theta' &= D^*_{13} M + D^*_{33} \tau
\end{aligned}
$$

where

$$
T = 1/\nu \int_r^1 m r dr. \qquad (1)
$$

is the local tension. D_{ij}^* $(i,j=1,3)$ are the structural complience coefficients, m is the running mass, k_θ is the cross-section radius of gyration and $\nu=m\Omega^2R^4/EI_{ref}$. F_w and M_θ are the aerodynamic running force and moment, respectively. This set of six first-order differential equations may be discretized in space by defining the blade local properties as the elements of diagonal matrices of dimension n. These elements are treated during the integration process as constants that spatially weight the dependent variable to be integrated. The rows of the integrating (or differentiating) operator define the weighting numbers associated with the interpolating polynomial used in the integration. Thus, pre-multiplication of a dependent variable described by a discrete vector **f** of dimension *nx1* by h**WC** (where **W** is the matrix of polynomial weighting numbers, **C** is the diagonal matrix of local properties and h is the length of the integration step) yields an approximation for one generic element of area under the curve **Cf**. Further defining **S** as a lower triangular matrix of ones ($S_{ij}=1$ when $i \geq j$ and $S_{ij}=0$ if $i<j$), the product h**SWCf** produces a *nx1* vector such that its i^{th} element is the

integral of **f** from the first to the i^{th} point along the integration path. An integration constant **k** associated with the value of **f** at the first point along the path is naturally obtained. Moreover, the integration can be carried out in the two directions along the path, allowing the association of **k** with any of the two boundary conditions. The integrating matrix operator **L** is defined by the product *h***SW**. Hence, a set of differential equations such as Eq. 1 is formally integrated in space by (1) pre-multiplication of each term by the integrating matrix operator **L**, and (2) evaluation of the corresponding integration constants using the given boundary conditions. In the present analysis those associated with a bearingless rotor are used:

$$\begin{aligned} &M(0) = c_\varphi \varphi(0) \\ &M(R) = 0 \\ &H(R) = 0 \\ &w(0) = 0 \\ &\tau(R) = 0 \\ &\tau(0) = c_\theta(\theta(0) - \theta_c). \end{aligned} \tag{2}$$

The parameters c_φ and c_θ define the blade root flexibility in bending and torsion, respectively. Both the collective (θ_0) and cyclic (θ_1) pitch control angles are introduced through the single input variable

$$\theta_c = \theta_0 + \theta_{1c}\cos\psi + \theta_{1s}\sin\psi \tag{3}$$

dependent on the azimuth angle. Since by definition the first row of the integrating matrix operator is composed of zeros (**Cf** is integrated from the first point to itself), and the last row represents the integral of **Cf** from the first to the last discretizing point of the normalized interval ($1 \geq r \geq 0$), it is possible to define two square matrices of size n

$$\mathbf{B}_0 = \begin{bmatrix} 1 & 0 & \cdots & 0 \\ 1 & 0 & \cdots & 0 \\ \vdots & \vdots & \cdots & \vdots \\ 1 & 0 & \cdots & 0 \end{bmatrix}; \mathbf{B}_1 = \begin{bmatrix} 0 & 0 & \cdots & 1 \\ 0 & 0 & \cdots & 1 \\ \vdots & \vdots & \cdots & \vdots \\ 0 & 0 & \cdots & 1 \end{bmatrix} \tag{4}$$

such that

$$\mathbf{B}_0\mathbf{L} = \mathbf{0}; \mathbf{B}_0\mathbf{f} = \mathbf{f}(0) = \mathbf{k}; \mathbf{B}_1\mathbf{f} = \mathbf{f}(1) = \mathbf{k}. \tag{5}$$

Hence, the solution proceeds by (1) pre-multiplying each (already integrated) member of Eq. 1 by either $\mathbf{B}_0$ or $\mathbf{B}_1$, and (2) observing the boundary conditions in Eq. 2. The six integration constants are isolated, respectively:

$$
\begin{aligned}
\mathbf{k}_M &= -\mathbf{B}_1\mathbf{L}H - \nu\mathbf{B}_1\mathbf{L}\tilde{T}\varphi \\
\mathbf{k}_H &= -\nu\mathbf{B}_1\mathbf{L}\tilde{m}\ddot{w} + \mathbf{B}_1\mathbf{L}F_w \\
\mathbf{k}_\varphi &= 1/c_\varphi\mathbf{k}_M \\
\mathbf{k}_w &= \mathbf{0} \\
\mathbf{k}_\tau &= -\nu\mathbf{B}_1\mathbf{L}\tilde{m}\tilde{k}_\theta^2(\theta+\ddot{\theta}) + \mathbf{B}_1\mathbf{L}M_\theta \\
\mathbf{k}_\theta &= 1/c_\theta\mathbf{k}_\tau + \mathbf{1}_{n\times 1}\theta_c.
\end{aligned}
\tag{6}
$$

The constants are substituted back in Eq. 1 (integrated) and the resulting equations are algebraically manipulated in order to reduce the order of the problem, yielding

$$
\mathbf{F}\dot{\mathbf{x}} - \mathbf{x} = \mathbf{G}\mathbf{x} + \mathbf{H}\mathbf{u}, \tag{7}
$$

where

$$
\mathbf{x} = \begin{bmatrix} \varphi & \theta & \dot{\varphi} & \dot{\theta} \end{bmatrix}^T \tag{8}
$$

$$
\mathbf{F} = \begin{bmatrix} \mathbf{0} & -\nu\mathbf{L}_\mathbf{D}\mathbf{L}_\mathbf{M} \\ \mathbf{1} & \mathbf{0} \end{bmatrix}; \mathbf{G} = \begin{bmatrix} \nu\mathbf{L}_\mathbf{D}\mathbf{Z} & \mathbf{0} \\ \mathbf{0} & \mathbf{0} \end{bmatrix}; \mathbf{H} = \begin{bmatrix} \mathbf{H}_1 & \nu\gamma\mathbf{H}_2 \end{bmatrix} \tag{9}
$$

$$
\mathbf{L}_\mathbf{D} = \begin{bmatrix} \mathbf{L}\tilde{D}^*_{11}\mathbf{L}^* + 1/c_\varphi\mathbf{B}_1\mathbf{L} & \mathbf{L}\tilde{D}^*_{13}\mathbf{L}^* \\ \mathbf{L}\tilde{D}^*_{13}\mathbf{L}^* & \mathbf{L}\tilde{D}^*_{33}\mathbf{L}^* + 1/c_\theta\mathbf{B}_1\mathbf{L} \end{bmatrix}; \mathbf{L}_\mathbf{M} = \begin{bmatrix} \mathbf{L}\tilde{m}\mathbf{L} & \mathbf{0} \\ \mathbf{0} & \tilde{m}\tilde{k}_\theta^2 \end{bmatrix} \tag{10}
$$

$$
\mathbf{Z} = \begin{bmatrix} \tilde{T} & \mathbf{0} \\ \mathbf{0} & \tilde{m}\tilde{k}_\theta^2 \end{bmatrix}; \mathbf{H}_1 = -\begin{bmatrix} \mathbf{0}_{n\times 1} \\ \mathbf{1}_{n\times 1} \end{bmatrix}; \mathbf{H}_2 = -\mathbf{L}_\mathbf{D}\begin{bmatrix} \mathbf{L}^* & \mathbf{0} \\ \mathbf{0} & \mathbf{1} \end{bmatrix} \tag{11}
$$

$$
\mathbf{u} = \begin{bmatrix} \theta_c & -F_w & M_\theta \end{bmatrix}^T. \tag{12}
$$

and γ is the Lock number. In Eqs. 10-11 $\mathbf{L}^*$ is the integrating matrix in the backward direction,

$$
\mathbf{L}^*\mathbf{f} = (\mathbf{B}_1 - \mathbf{1})\mathbf{L}\mathbf{f} = \int_r^1 \mathbf{f}dr. \tag{13}
$$

The left hand side of Eq. 7 defines the eigenvalue problem associated with a non-rotating beam having the mass and stiffness properties of the blade:

$$\mathbf{F}\mathbf{U}_r = \mathbf{U}_r \Lambda^{-1}. \tag{14}$$

Since the **L** operator is not symmetric, the eigenvectors collected in the columns of $\mathbf{U}_r$ are not real quantities. Furthermore, they are orthogonal to their respective *left* eigenvectors, obtained by solving the eigenvalue problem associated with the transpose of **F** in Eq. 14. Alternatively, the left modal matrix is calculated by the pseudo-inverse of $\mathbf{U}_r$ (Eq. 15, where the superscript H denotes the Hermitian transpose). This is a preferred method if the modal subspace is truncated after the first *m* natural modes. In the diagonal matrix of eigenvalues the natural frequencies (normalized by Ω) appear in the imaginary part of the roots, and always as a pair of complex conjugate numbers. Both the *right* and *left* eigenvectors also appear in complex conjugate pairs. Viscous damping can be introduced at this point by adding a real part to the roots in Λ.

$$\mathbf{U}_l = (\mathbf{U}_r{}^H \mathbf{U}_r)^{-1} \mathbf{U}_r{}^H. \tag{15}$$

The following *bi-orthogonal* identities hold for the modal matrices:

$$\mathbf{U}_l \mathbf{U}_r = \mathbf{1}; \Lambda = (\mathbf{U}_l \mathbf{F} \mathbf{U}_r)^{-1}. \tag{16}$$

Matrix **G** in Eq. 7 contains the geometric stiffness terms generated by the spinning blade, and the product **Hu** the external loads due to both the blade control system and aerodynamics. Therefore, the system's single input variable becomes the azimuth angle, i.e.: $\mathbf{u}=\mathbf{u}(\psi)$. The aerodynamic loads are obtained through an independent calculation in the present study, assuming a rigid blade subject to the same flight conditions of the elastic blade. In steady-state regime the unsteady aerodynamic coefficients are periodic functions of the azimuth angle and may be expanded in Fourier series:

$$c_M = \frac{1}{2} c_{M_0} + \sum_{k=1}^{l-1} (c_{M_{ck}} \cos k\psi + c_{M_{sk}} \sin k\psi); c_L = \frac{1}{2} c_{L_0} + \sum_{k=1}^{l-1} (c_{L_{ck}} \cos k\psi + c_{L_{sk}} \sin k\psi), \tag{17}$$

where *l* is taken to achieve the series convergence. The latter coefficients are related to the aerodynamic loads in Eq. 12 by

$$F_w = -\frac{1}{2} u^2 c_L; M_\theta = \frac{1}{2} (c/R) u^2 c_M. \tag{18}$$

In Eq. 18 the cross-section's normalized local velocity is approximated by its tangential component,

$$u \cong u_T = r + \mu \sin \psi \tag{19}$$

where c is the blade chord and μ the advance ratio. In general, the Fourier coefficients are complex quantities (if the aerodynamic damping is considered in the analysis), yielding:

$$c_M = c_M{}' + ic_M{}'' ; c_L = c_L{}' + ic_L{}''. \tag{20}$$

The aerodynamic moment coefficient c_M is calculated with respect to the elastic axis, i.e. $c_M = c_{M_{1/4}} - (0.25 - x_{EA})c_L$, where the elastic axis position x_{EA} is measured in chords from the airfoil leading edge aft.

In order to further reduce the order of the problem, it is convenient to decompose Eq. 7 in the modal subspace spanned by the blade normal modes (non-spinning condition). In so doing, the geometric stiffness terms are treated as external loads as well. Using the transformation

$$\mathbf{x} = \mathbf{U}_r \eta \tag{21}$$

and Eq. 16, one gets

$$\dot{\eta} = \mathbf{A}\eta + \mathbf{B}\mathbf{u}, \tag{22}$$

where

$$\mathbf{A} = \Lambda(\mathbf{1} + \mathbf{U}_l \mathbf{G} \mathbf{U}_r); \mathbf{B} = \Lambda \mathbf{U}_l^1 \mathbf{H}. \tag{23}$$

The superscript 1 on the left modal matrix denotes its upper half partition (of dimension *mx2N*).

The system's output can be either the vector of physical dependent variables (using Eq. 21) or the reaction loads at the blade root (shear resultant and torque). The former gives the distributed elastic displacement field along the blade (bending slope and torsion), whereas the latter is particularly interesting because these are precisely the dynamic loads transmitted into the helicopter's airframe due to the blade aeroelastic response. The blade root reactions can be calculated observing Eqs. 1, 5 and 6:

$$\begin{aligned} H(0) &= \mathbf{k}_H ; \ddot{w} = -\mathbf{L}\ddot{\varphi} \\ \tau(0) &= \mathbf{k}_\tau . \end{aligned} \tag{24}$$

Partitioning the right modal matrix into its four *Nxm* components (numbered with the superscripts 1 to 4), taking the necessary time derivatives in Eq. 21,

$$\ddot{\varphi} = \mathbf{U}_r{}^3 \dot{\eta}; \theta = \mathbf{U}_r{}^2 \eta; \ddot{\theta} = \mathbf{U}_r{}^4 \dot{\eta} \tag{25}$$

and substituting Eq. 22 into the first and third equations in Eq. 25, the following is obtained:

$$\begin{Bmatrix} \ddot{\varphi} \\ \theta \\ \ddot{\theta} \end{Bmatrix} = \begin{bmatrix} \mathbf{U_r}^3\mathbf{A} \\ \mathbf{U_r}^2 \\ \mathbf{U_r}^4\mathbf{A} \end{bmatrix} \eta + \begin{bmatrix} \mathbf{U_r}^3\mathbf{B} \\ \mathbf{0} \\ \mathbf{U_r}^4\mathbf{B} \end{bmatrix} \mathbf{u}. \tag{26}$$

From Eq. 24,

$$\begin{Bmatrix} H(0) \\ \tau(0) \end{Bmatrix} = \nu \begin{bmatrix} \mathbf{B_1 L} \grave{m} \mathbf{L} & \mathbf{0} & \mathbf{0} \\ \mathbf{0} & -\mathbf{B_1 L} \grave{m} \grave{k}_\theta^2 & -\mathbf{B_1 L} \grave{m} \grave{k}_\theta^2 \end{bmatrix} \begin{Bmatrix} \ddot{\varphi} \\ \theta \\ \ddot{\theta} \end{Bmatrix} + \nu\gamma \begin{bmatrix} \mathbf{B_1 L} & \mathbf{0} \\ \mathbf{0} & \mathbf{B_1 L} \end{bmatrix} \mathbf{u}. \tag{27}$$

Substitution of Eq. 26 into Eq. 27 yields

$$\mathbf{y} = \begin{Bmatrix} H(0) \\ \tau(0) \end{Bmatrix} = \mathbf{C}\eta + \mathbf{D}\mathbf{u}, \tag{28}$$

which is the standard form of the output equation.

3. A Case Study

The aeroelastic response of the 40%-scaled, BO-105's two meter diameter four blade rotor model that was tested in the German-Dutch Wind Tunnel (DNW) in December 1992 is investigated. A thoroughly description of the test may be found in [5]. The blades were instrumented to measure among other parameters the pressure distribution along the structure, providing a check for aerodynamic calculations. However, high aeroelastic response was observed during the tests because for the sake of the reliability the blade specimens were as flexible as actual helicopter blades. The tests were conducted to simulate real situations in lifting forward flight. For this, rotor pitch and tilt angle control facilities were introduced in the apparatus.

The aerodynamic model used in the present analysis is due to Ahmed and Vidjaja [6]. It is a 3-D unsteady panel method developed to numerically compute the subsonic aerodynamics of finite thickness multi-blade rotors including dynamic stall, compressibility and free wake. The free wake is simulated by a lattice of shed and trailing vortices. Since no restrictions are placed on the prescribed blade control, blade profile, planform, twist, etc., the code can treat multi-blade rotors in a variety of flight conditions including the descent and climb modes. Although a rigid blade was assumed, prediction of pressure distribution on the blade surface in the hover situation agreed very well with the wind tunnel test data; results for the descent flight are also in fair agreement with the experiment.

After the periodic regime is established, the aerodynamic loads associated with a *rigid* blade

$$c_L = c_L(\psi;\mu,\theta_c,\alpha,k,M_{\Omega R},c_T)$$
$$c_{M_{1/4}} = c_{M_{1/4}}(\psi;\mu,\theta_c,\alpha,k,M_{\Omega R},c_T) \tag{29}$$

are introduced into the *aeroelastic* model associated with the same flight condition (defined by the first three parameters in Eq. 29). Therefore, the last four parameters in Eq. 29 (respectively shaft tilt angle α, reduced frequency k, tip Mach number $M_{\Omega R}$ and thrust coefficient c_T) are not *explicit* variables in the aeroelastic model. The reduced frequency is based on the rotor spinning frequency. If the periodic regime is already established (to assure the series convergence and avoid the so-called Gibbs effect [7]), the aerodynamic coefficients may be expanded in Fourier series (Eq. 17). For this, the following operation is performed:

$$\mathbf{c}_{\mathbf{L}_s} = \frac{2}{n^*}\begin{bmatrix} 0 & 0 & 0 & \cdots & 0 \\ 0 & \sin\frac{1}{n^*-1}2\psi & \sin\frac{2}{n^*-1}2\psi & \cdots & \sin\frac{n^*-1}{n^*-1}2\pi \\ 0 & \sin\frac{1}{n^*-1}4\psi & \sin\frac{2}{n^*-1}4\psi & \cdots & \sin\frac{n^*-1}{n^*-1}4\pi \\ \vdots & \vdots & \vdots & \vdots & \vdots \\ 0 & \sin\frac{1}{n^*-1}2(l-1)\psi & \sin\frac{2}{n^*-1}2(l-1)\psi & \cdots & \sin\frac{n^*-1}{n^*-1}2(l-1)\pi \end{bmatrix}_{l\times n^*} \mathbf{c}_{\mathbf{L}} \tag{30a}$$

$$\mathbf{c}_{\mathbf{L}_c} = \frac{2}{n^*}\begin{bmatrix} 1/2 & 1/2 & 1/2 & \cdots & 1/2 \\ 1 & \cos\frac{1}{n^*-1}2\psi & \cos\frac{2}{n^*-1}2\psi & \cdots & \cos\frac{n^*-1}{n^*-1}2\pi \\ 1 & \cos\frac{1}{n^*-1}4\psi & \cos\frac{2}{n^*-1}4\psi & \cdots & \cos\frac{n^*-1}{n^*-1}4\pi \\ \vdots & \vdots & \vdots & \vdots & \vdots \\ 1 & \cos\frac{1}{n^*-1}2(l-1)\psi & \cos\frac{2}{n^*-1}2(l-1)\psi & \cdots & \cos\frac{n^*-1}{n^*-1}2(l-1)\pi \end{bmatrix}_{l\times n^*} \mathbf{c}_{\mathbf{L}} \tag{30b}$$

where

$$\mathbf{c}_{\mathbf{L}} = \mathbf{c}_{\mathbf{L}}(i,j); i = 1,\ldots n^*; j = 1,\ldots n \tag{31}$$

is a matrix in which each column gives a fine discretization of the lift coefficient at the j^{th} r/R station along the blade (n^* is typically a large value in the order of 10^3). The matrix $\mathbf{c}_L(\psi,r/R)=\mathbf{c}_L(\psi+2\pi,r/R)$ is directly obtained from the aerodynamic model output data. A similar calculation can be made for the moment coefficient. Once the coefficient matrices in Eqs. 30a-b are obtained, the external loads in the modal subspace can be efficiently integrated since at each time step (corresponding to an azimuth angle) the vector $\mathbf{u}$ is computed from

$$\mathbf{u} = \begin{Bmatrix} \theta_c \\ \mathbf{1}_{1\times l}(\mathbf{C}_k\mathbf{c}_{L_c} + \mathbf{S}_k\mathbf{c}_{L_s})^T \\ \mathbf{1}_{1\times l}(\mathbf{C}_k\mathbf{c}_{M_c} + \mathbf{S}_k\mathbf{c}_{M_s})^T \end{Bmatrix}, \tag{32}$$

where

$$\mathbf{C}_k = \begin{bmatrix} 1 & & \\ & \cos\psi & \\ & & \ddots \\ & & \cos(l-1)\psi \end{bmatrix}; \mathbf{S}_k = \begin{bmatrix} 0 & & \\ & \sin\psi & \\ & & \ddots \\ & & \sin(l-1)\psi \end{bmatrix}. \tag{33}$$

The present case-study is based in the parameters listed in Table 1.

Table 1: Aerodynamic parameters

Parameter	Value
$M_{\Omega R}$	.74
c_T	.00448
α	5.05 (deg)
θ_r	3.83+1.68cosψ-1.01sinψ (deg)
μ	.15
mode	descent

Four typical results from the Fourier series expansion using 20 terms are depicted in Figs. 1-4 for the azimuth angles 0, 90, 157.5 and 225 degrees, indicating that a very good approximation is obtained at least for the lift coefficient. It was verified that an equivalent convergence for the aerodynamic moment coefficient requires the minimum of 40 Fourier terms. In the present analysis *l=20* was considered satisfactory.

Optimization techniques were used to match the blade's natural eigenfrequencies under 100 Hz obtained by solving the eigenvalue problem represented by Eq. 14 to the experimental free-vibration test conduct at DLR-WB-AE in Göttingen. The results are presented in Table 2. In Table 3, the eigenfrequencies for the full-speed rotating blade calculated using the present scheme are compared to those obtained with CAMRAD/JA. Since the present model does not include the lead-lag motion, the comparison can be considered excellent. The present analysis diverges from CAMRAD/JA in the torsion's mode prevision, but it leads to a more precise result with respect to the conducted tests (CAMRAD/JA modes were not optimized against experimental results).

Table 2: Natural Frequencies from the BO-105 Model (in Hz)

Mode Number	Experiment	CAMRAD/JA	Present	Description
1	2.43	2.50	2.43	1st flap
2	9.49	9.75	-	1st lead-lag
3	13.92	15.25	13.92	2nd flap
4	35.42	40.00	37.39	3rd flap
5	55.68	65.25	55.68	1st torsion
6	60.69	60.00	-	2nd lead-lag
7	70.19	78.50	70.19	4th flap

Table 3: Modal Frequencies at Nominal Spinning Frequency: 110 rad/s (in Hz)

Mode Number	Present	CAMRAD/JA
1	19.6	20
3	48.2	47
4	85.8	83
5	58.4	68
7	127	N/A

4. Results

The aeroelastic simulations were performed in a 486DX2/66MHz personal computer using the Matlab-Simulink™ software. The system consisting of Eq. 22 and either Eq. 21 or Eq. 28 was integrated in the time domain using the fifth-order with fourth-order step-size control Range-Kutta "rk45" built-in routine. Since no provision for the integration of a complex-valued problem is made in Matlab, the system's size was doubled by defining real-valued matrices in the form

$$\tilde{\mathbf{A}} = \begin{bmatrix} \mathrm{Re}(\mathbf{A}) & -\mathrm{Im}(\mathbf{A}) \\ \mathrm{Im}(\mathbf{A}) & \mathrm{Re}(\mathbf{A}) \end{bmatrix}. \tag{34}$$

The integration is carried out until steady-state solutions are obtained. A typical integration up to 8 complete blade revolutions takes less than 30 seconds CPU time, which confirms that the model has the potential to be coupled with the aerodynamic code in future on-line aeroelastic simulations. Five natural modes (numbers 1, 3, 4, 5, 7 in Table 2) were used to construct the modal subspace. The fifth-order Newton integrating matrix with n=10 discretizing points was employed in the solution. The imaginary part of the aerodynamic coefficients (aerodynamic damping due to the out-of-phase motion in Eq. 20) was neglected in the present analysis.

Figures 5 and 6 present the power-spectral-density (PSD) plots (averaged over 1024 points) for the elastic deflections in bending and torsion at the station r/R=1.0, respectively. They represent the situation without the introduction of viscous damping. From the two figures one can observe the peaks corresponding to aerodynamic modes at multiples of the blade revolution frequency. The amplitude of those "aerodynamic

peaks" decreases to a residual value as the frequency increases, indicating that in fact a satisfactory Fourier series convergence was achieved with 20 terms. Furthermore, the series convergence is much faster in the case of the bending-related plot, a result that confirms the behavior of the lift and aerodynamic moment coefficients in Figs 1-4. In Figs. 5 and 6, the dynamic contribution is restricted to the interval below 10/rev due to the assumed modal truncation. The "dynamic peaks" correspond to the frequencies associated with the spinning blade eigenfrequencies. It is worthwhile to observe the proximity of some of the latter peaks with respect to the "aerodynamic peaks" (as between the 1st bending and the 1/rev frequency, the 2nd bending and the 3/rev frequency, the 3rd bending and the 5/rev frequency, the 1st torsion and the 3/rev frequency). The proximity between "dynamic" and "aerodynamic peaks" leads in the present model to the well-known *beat phenomenon*, where the amplitude of the motion is modulated according to a much lower frequency (the difference between the two frequencies), as one can confirm by observing Figs. 7 and 8 (for the bending and torsion at r/R=.5555, respectively. The phenomenon is observed throughout the entire blade span). If viscous damping is artificially included (10%), the phenomenon disappears (Figs. 9 and 10) and only the unchanged "aerodynamic peaks" remain (Figs. 11 and 12). Although the amplitudes of the peaks at the multiples of blade frequency are obviously the same (in the present model the aerodynamic loads are decoupled from the system's dynamics), the PSD plots prove that the energy content at *off resonance* frequencies is much reduced. The 4/rev frequency matches the first harmonic of the number of blades and thus can be considered critical. Much of the energy content of the PSD's spectrum in the neighborhood of 4/rev is transmitted into the helicopter's airframe in the form of mechanical vibration. Passive and active control techniques (Higher Harmonic Control - HHC - and Individual Blade Control - IBC) were devised to deal with the problem. Of course, in an aeroelastic model where the feedback between aerodynamic and dynamic loads is present the distinction between "dynamic" and "aerodynamic" modes is not as clear as in the present formulation. Aeroelastic modes are dominant, instead. However, a deeper insight into the phenomena associated with the helicopter rotor vibration can be acquired in a simple model such as this. It becomes clear that controlling the blade *aeroelastic* modes at frequencies near to the 4/rev frequency by adding either artificial damping or stiffness to the blade structure the overall level of vibration of the airframe/rotor system is greatly attenuated.

Figures 13 and 14 depict the results obtained for the reaction loads at the blade root. The spectrum closely resembles their counterparts in blade displacement variables because no coupling between bending and torsion is introduced by Eq. 27. However, the latter results are useful if a complete rotor model is to be built afterwards.

5. Conclusions

From the present investigation some conclusions can be drawn:

- A computational efficient method to analyze the forced response of helicopter bearingless rotors including important aerodynamic effects such as dynamic stall, compressibility and free wake is developed. The method is suitable to include both multi-blade analyses and closed-loop active control without loosing its performance.
- The proximity between "dynamic" and "aerodynamic" modes greatly increases the aeroelastic response at off-resonance frequencies. The beat phenomenon can be

observed if the modal frequencies are close enough and no significant damping is provided.
- Adding artificial structural damping and/or stiffness to the blade's aeroelastic modes can be beneficial to cure airframe/rotor high dynamic response in the vicinity of critical frequencies such as N/rev, where N is the number of blades.

6. Acknowledgement

The author would like to thank Dr. S. Ahmed from DLR's Institute of Design Aerodynamics for making available his aerodynamic calculations for the BO-105 rotor.

References

1. Nitzsche, F. and Breitbach, E., "A Study on the Feasibility of Using Adaptive Structures in the Attenuation of Vibration Characteristics of Rotary Wings," *Proceedings: AIAA/ASME/ASCE/AHS/ASC 33rd Structures, Structural Dynamics and Materials Conference,* AIAA, Washington DC, USA, 1992, Part 3, pp. 1391-1402 (to appear, *J. of Aircraft,* Nov/Dec. 1994?).
2. Nitzsche, F, Lammering, R. and Breitbach, E., "Cab Smart Materials Modify Blade Root Boundary Conditions to attenuate Helicopter Vibration?" *Proceedings: Fourth International Conference on Adaptive Structures,* Technomic Publishing Co., Cologne, Germany, November 2-4, 1993, pp. 139-150.
3. Lehman, L. L., "Hybrid State Vector Methods for Structural Dynamic and Aeroelastic Boundary Value Problems," NASA CR-3591, August 1982.
4. Nitzsche, F., "Designing Efficient Helicopter Individual Blade Controllers using Smart Structures," *Proceedings: AIAA/ASME Adaptive Structures Forum 1994,* AIAA, Washington DC, USA, 1994, pp. 298-308.
5. Splettstoesser, W. R, et al, "Experimental Results of the European HELINOISE Aeroacustic Rotor Test in the DNW," 19th European Rotorcraft Forum, Paper B8, Cernobbio, Italy, September 14-16, 1993.
6. Ahmed, S. R. and Vidjaja, V. T., "Unsteady Panel Method Calculation of Pressure Distribution on BO 105 Model Rotor Blades and Validation with DNW-Test Data, " *Proceedings: American Helicopter Society 50th Annual Forum,* AIAA, Washington DC, USA, May 11-13, 1994.
7. Ferziger, J. H., *Numerical Methods for Engineering Application,* John Wiley & Sons, New York, 1981, pp. 207-212.

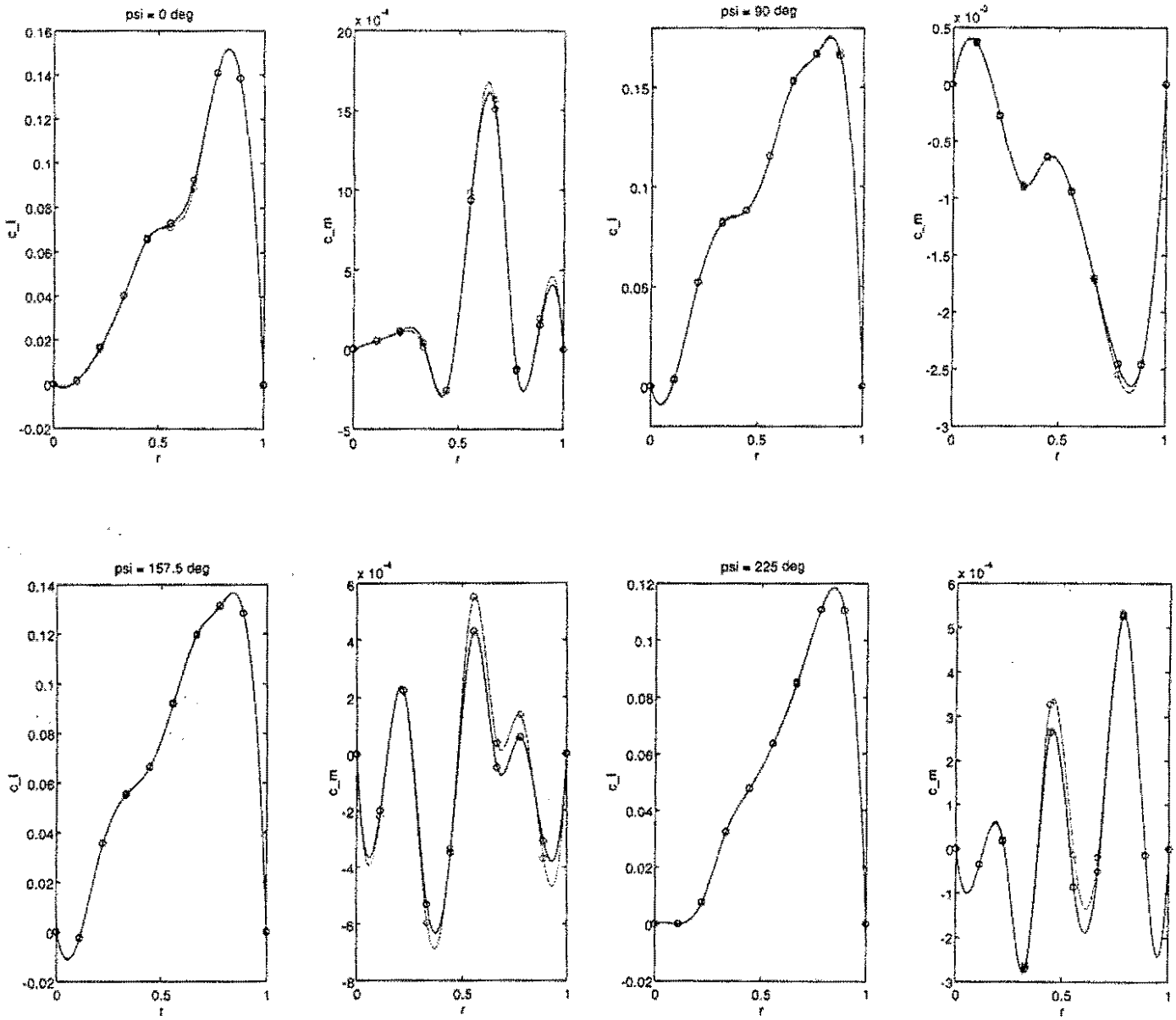

Figs. 1-4 From top to bottom, left to right: c_L and c_M (with respect to elastic axis) versus r/R for the azimuth angles ψ = 0, 90, 157.5 and 225 deg. The dashed lines correspond to the actual values; the solid lines to the Fourier series expansions using l=20 terms and n*=1000.

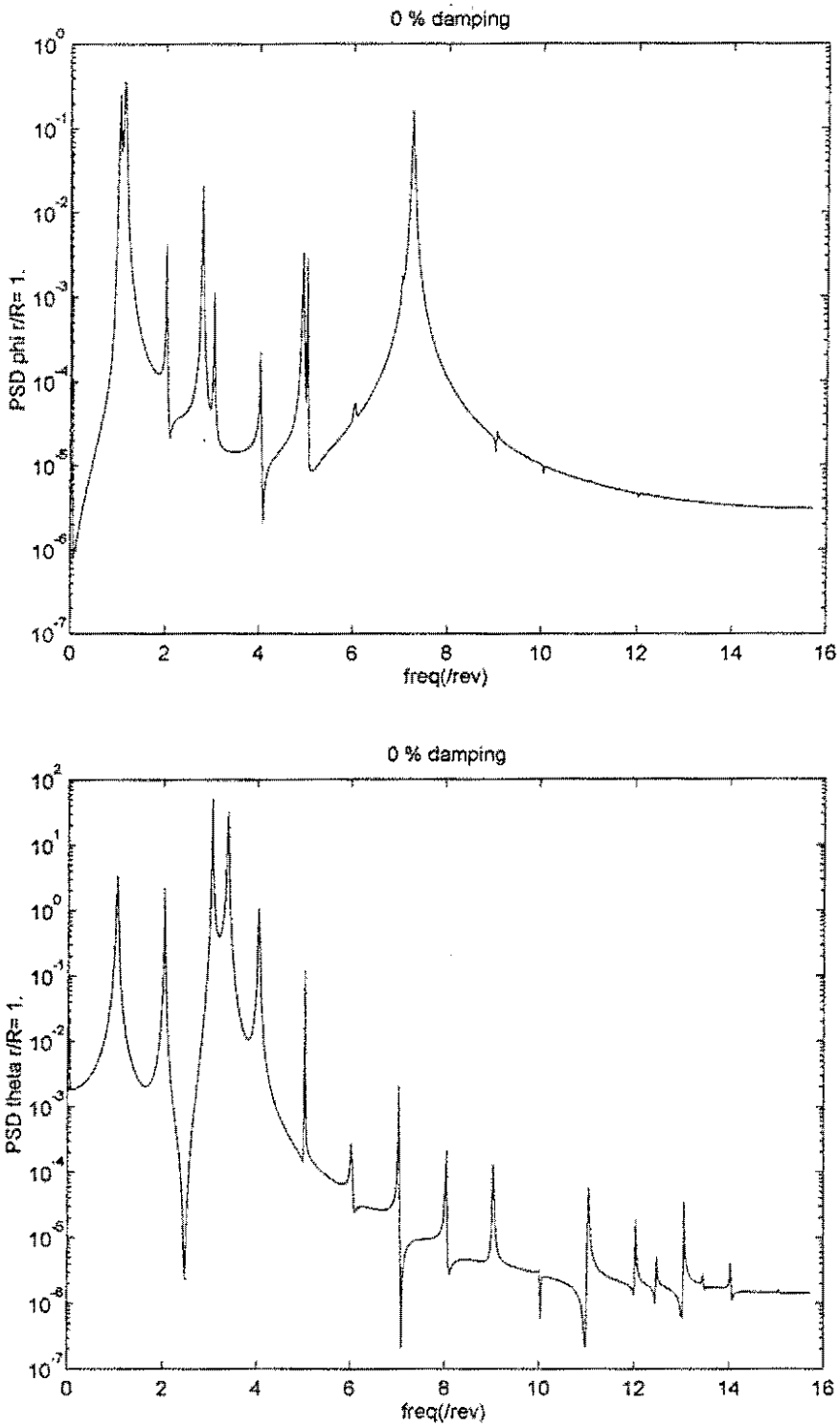

Figs. 5-6 Power spectral density plots of bending slope (top) and torsion angle (bottom) at the tip of the blade for the situation without viscous damping. The first five natural modes are used to represent the system's dynamics (under 100 Hz). Twenty harmonics of the blade spinning frequency are used to describe the aerodynamic loads.

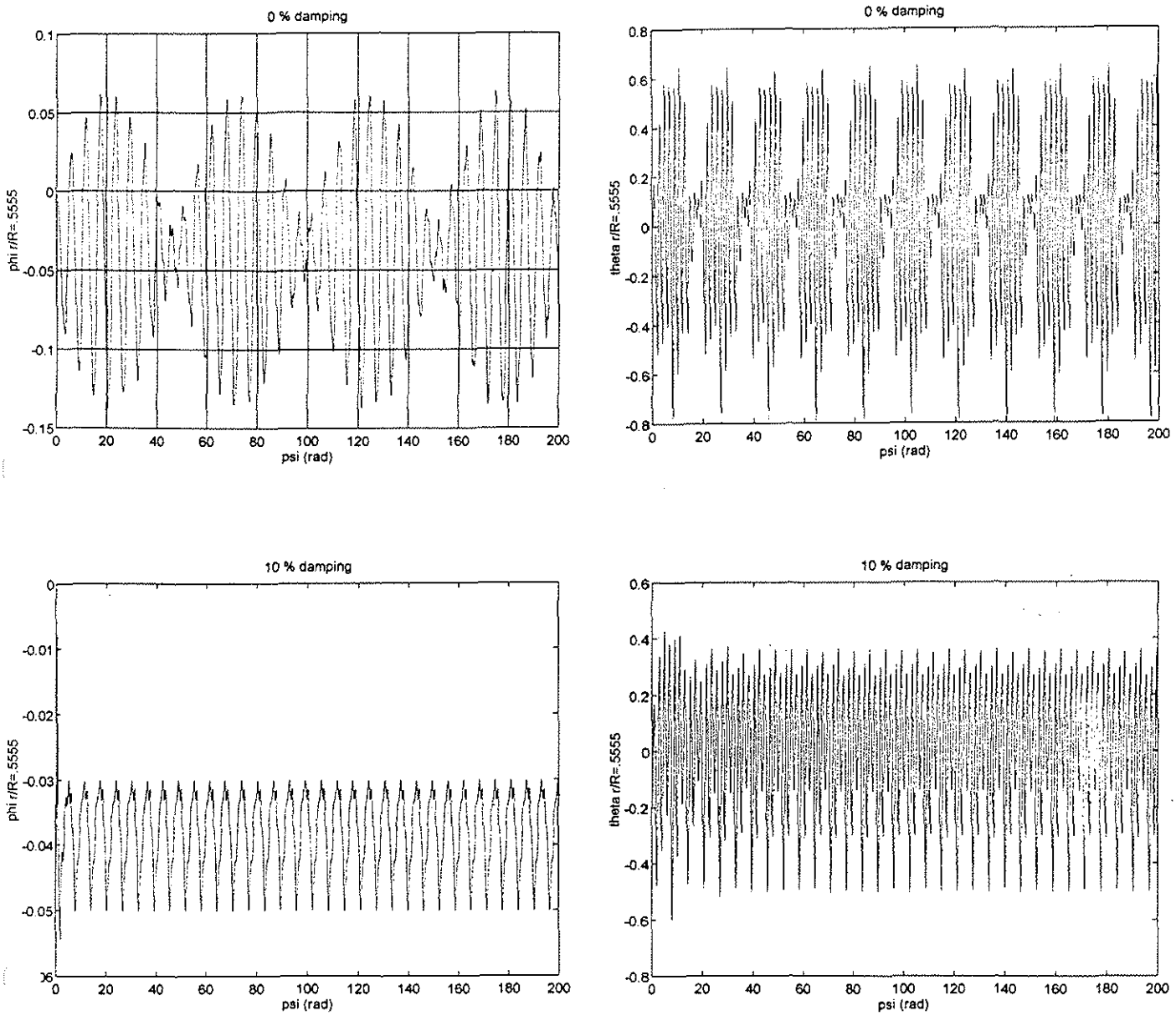

Figs. 7-10 From top to bottom, left to right: bending slope (left) and torsion angle (right) at the station r/R=0.5555 versus azimuth angle for the situations without damping (top) and with 10% of viscous damping (bottom). Time-domain simulations up to ψ = 200 rad (31 blade revolutions). The beat frequency is approximately 0.12/rev in the φ-mode and 0.37/rev in the θ-mode (situation without damping).

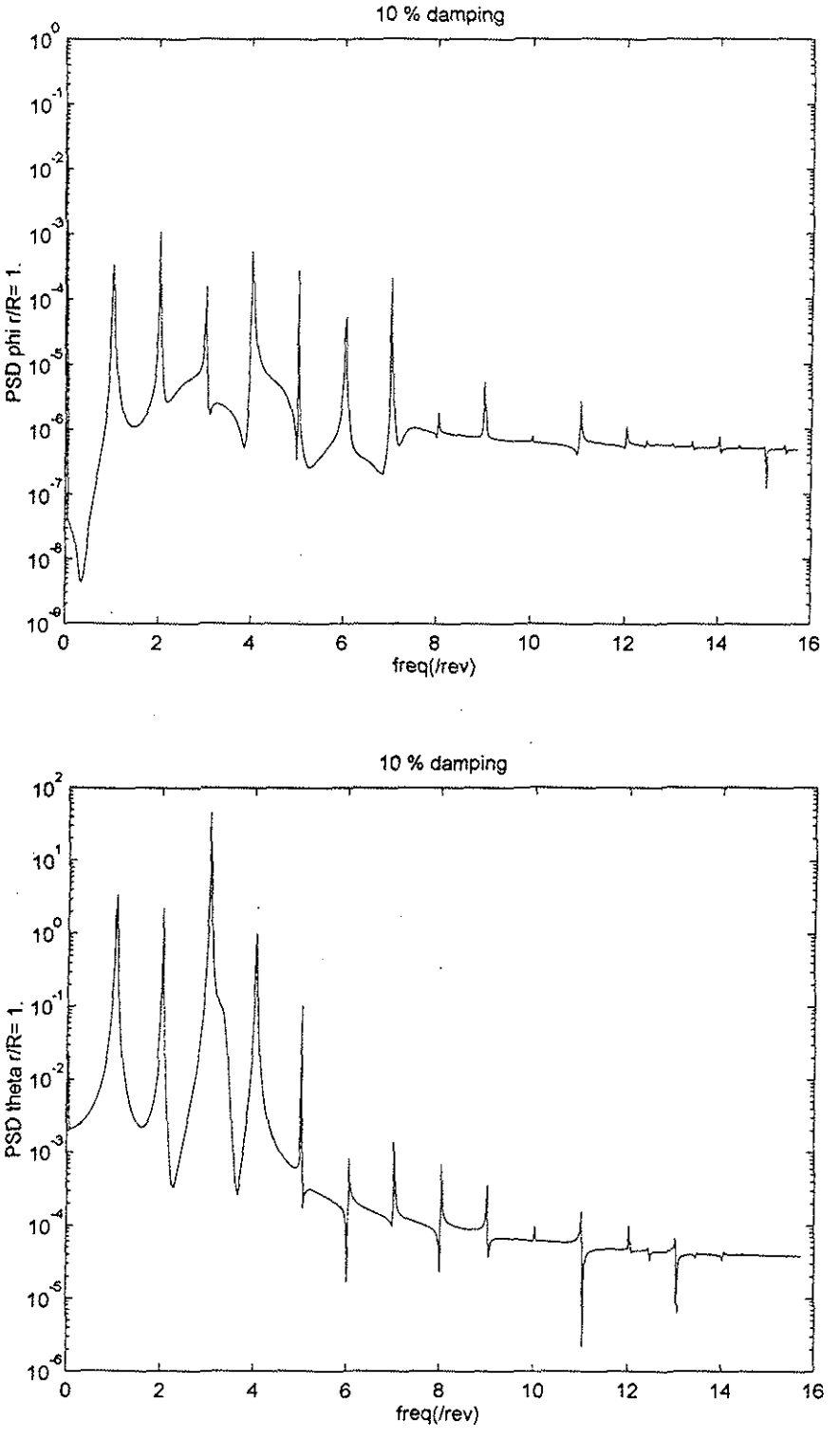

Figs. 11-12 Power spectral density plots of bending slope (top) and torsion angle (bottom) at the tip of the blade for the situation with 10% viscous damping. The first five natural modes are used to represent the system's dynamics (under 100 Hz). Twenty harmonics of the blade spinning frequency are used to describe the aerodynamic loads. Only the "aerodynamic modes" significantly contribute to the frequency spectrum. Off-resonance energy levels are much lower than those in the case of Figs. 5-6.

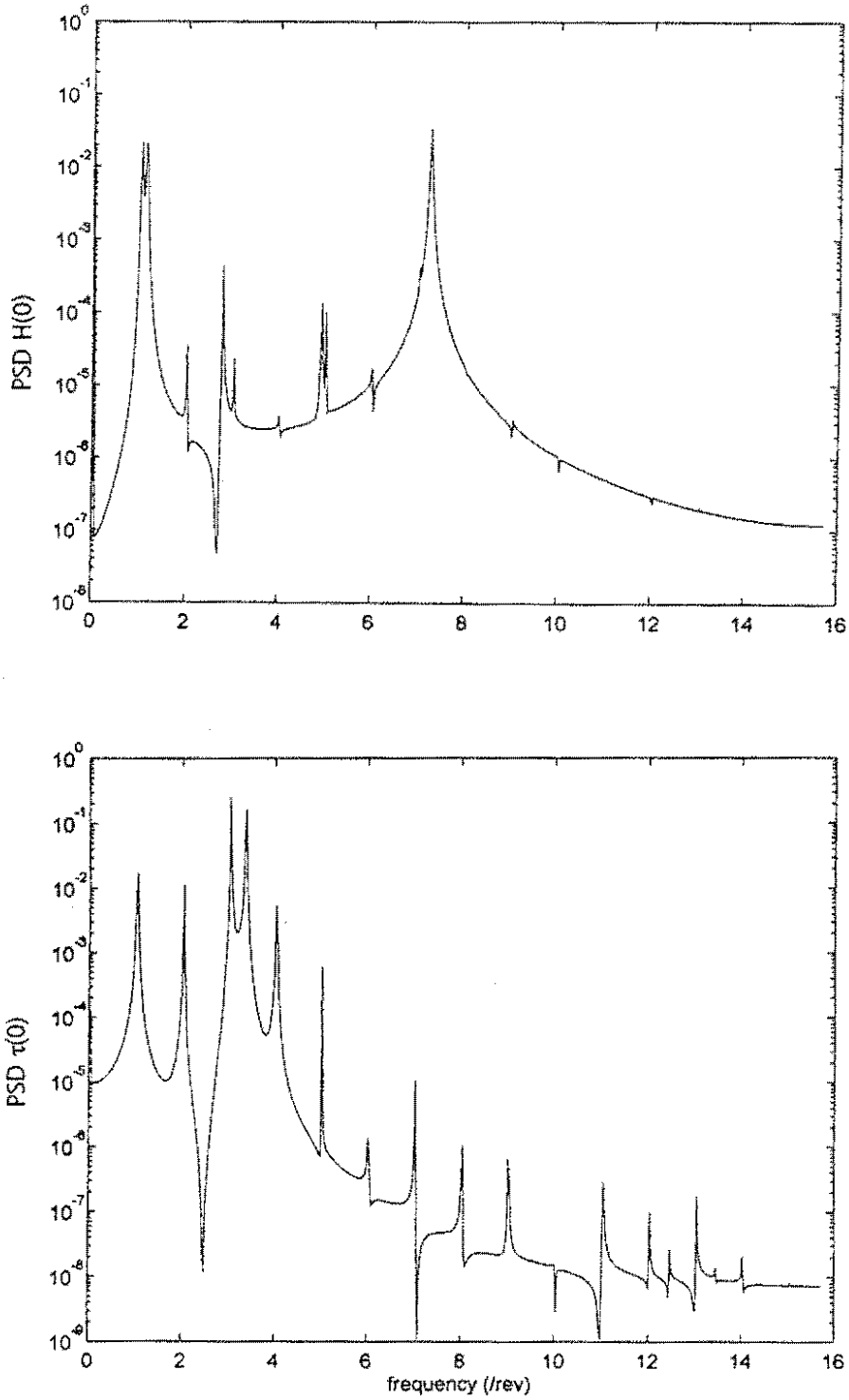

Figs. 13-14 Power spectral density plots of blade root reactions: bending shear (top) and torque (bottom).